

Strain-tunable Photonic Band Gap Microcavity Waveguides in Silicon at 1.55 μm

Chee Wei Wong^{*}, Xiaodong Yang^{*}, Peter T. Rakich⁺, Steven G. Johnson⁺,
Minghao Qi⁺, Yongbae Jeon⁺, George Barbastathis⁺, Sang-Gook Kim⁺
^{*}Columbia University, New York, NY 10027
⁺Massachusetts Institute of Technology, Cambridge, MA 02139
Email: cww2104@columbia.edu

The majority of photonic crystals developed till-date are not dynamically tunable, especially in silicon-based structures. Dynamic tunability is required not only for reconfiguration of the optical characteristics based on user-demand, but also for compensation against external disturbances and relaxation of tight device fabrication tolerances. Recent developments in photonic crystals have suggested interesting possibilities for static small-strain modulations to affect the optical characteristics¹⁻³, including a proposal for dynamic strain-tunability⁴. Here we report the theoretical analysis, device fabrication, and experimental measurements of tunable silicon photonic band gap microcavities in optical waveguides, through direct application of dynamic strain to the periodic structures⁵. The device concept consists of embedding the microcavity waveguide⁶ on a deformable SiO₂ membrane. The membrane is strained through integrated thin-film piezoelectric microactuators. We show a 1.54 nm shift in cavity resonances at 1.56 μm wavelengths for an applied piezoelectric strain of 0.04%. This is in excellent agreement with our modeling, predicted through first-order semi-analytical perturbation theory⁷ and finite-difference time-domain calculations. The measured microcavity transmission shows resonances between 1.55 to 1.57 μm , with Q factors ranging from 159 to 280. For operation at infrared wavelengths, we integrate X-ray and electron-beam lithography (for critical 100 nm feature sizes) with thin-film piezoelectric surface micromachining. This level of integration permits realizable silicon-based photonic chip devices, such as high-density optical filters and spontaneous-emission enhancement devices with tunable configurations.

1. INTRODUCTION

Tunable optical elements have been sought for active control against external disturbances, switching modules in integrated optics, and compensation for fabrication mismatches and tight process tolerances. We develop the concept of strain-tuning for periodic optical devices – such as diffractive gratings and photonic crystals – on a deformable membrane piezoelectrically actuated with sub-nanometer resolution as a means to achieve tunability. The strain-based approach to tuning of periodic optical elements is appealing for two reasons: (i) it provides the capability of tuning the performance of silicon microphotronics, where electro-optic effects are negligible and devices have commonly been tuned only by thermal means, and (ii) achieves ultra-fine resolution with low power and voltage requirements through piezoelectric actuators. Moreover, in contrast to thermal means, piezoelectric strain-tuning provides significantly faster response and better localization of tunability. Both devices we developed extend the concept of strain-tuning towards optical microelectromechanical systems (MEMS) and photonic crystals. In the tunable diffractive gratings, strain-tuning permits precise analog control of the diffraction angle on the order of a microradian. Prior work on “digital” tunable gratings involve the control of an individual grating beam or a set of beams [8,9]; previous demonstrations on analog tunable gratings involve either thermal actuation [10,11], or vertical and lateral movement of vertically stacked grating structures [11]. Compared to these tunable grating implementations, our device has shown a more precise angular resolution for a smaller tuning range [12].

In this work, we report on strain-tuning for photonic crystals to achieve sub-nanometer lattice deformations. Sub-nanometer strain tuning has many potential applications such as tunable low-threshold microlasers, filters and signal routers in silicon microphotronics. Effect of static strain on the periodic lattice of coupled vertical microcavity resonators has been reported [2] and a theoretical design for shear-modulated 2-dimensional photonic crystals on bulk piezoelectrics has been proposed [4]. Herein we present piezoelectric strain-tuning towards a 1D photonic band gap microcavity to achieve active tuning of the resonant frequency. The microcavity design we used is based on the work first reported by Foresi and coworkers [6].

The general design concept of the strain-tunable platform for microphotronics is illustrated in Figure 1. The platform is a double-anchored membrane made of either platinum or silicon-silica, and actuated by thin-film piezoelectric actuators. The applied strain is transferred to the optical element of interest; in particular, the 1D photonic band gap microcavity is described this paper. This dynamic strain permits active control of its defect resonance. The detailed design is presented in section 2 and the fabrication is detailed in section 3. Experimental results are presented in section 4 and section 5 concludes, presenting future opportunities developed by this research.

2. DESIGN

As shown in Figure 2a, the microcavity is formed by the introduction of a point defect into a periodic array of holes in the high-index contrast Si waveguide. The waveguide has sub-micrometer dimensions ($t = 176$ nm and $w = 541$ nm), is single-mode and sits on a low-index SiO₂ ridge ($t_{ox} = 296$ nm). The periodic structure, with lattice constant a , splits the lower order guided mode to form a photonic band gap. The introduction of a defect – by adding dielectric material between two holes at the center of the periodic structure – permits a spatially localized resonant state to exist in the band gap. The design has dimensions $a = 429$ nm, $a_d = 643$ nm, and $d = 189$ nm. The electric field distribution is found through 3D finite-difference time-domain (FDTD) computations. Figure 2b shows the electromagnetic energy distribution sliced through the middle of the microcavity. The observed strong field confinement gives a modal volume of $0.055 \mu\text{m}^3$, about $5(\lambda/2n)^3$, where λ is the resonant

wavelength and n the silicon refractive index. The microcavity quality factor Q , defined as $\lambda/\delta\lambda$ where $\delta\lambda$ is the full-width half-maximum of the microcavity transmission, is estimated to be 175. The band structure of the photonic crystal without the defect is illustrated in Figure 3a. Applications of the microcavity include high-density optical filters and spontaneous-emission enhancement devices.

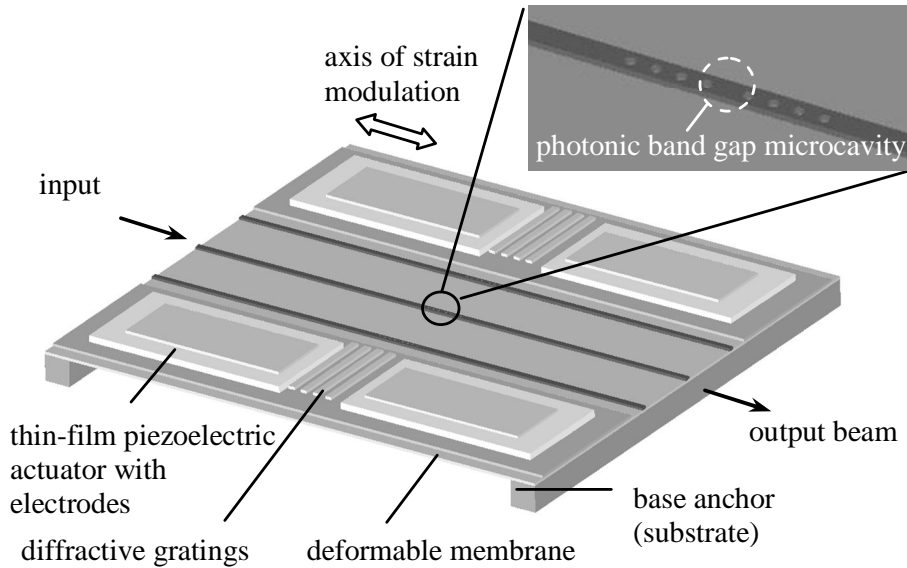


Fig. 1. Design schematic of the strain-tunable platform for microphotronics. A photonic band gap microcavity [6] is built on the deformable membrane. The membrane is actuated by thin-film piezoelectric actuators.

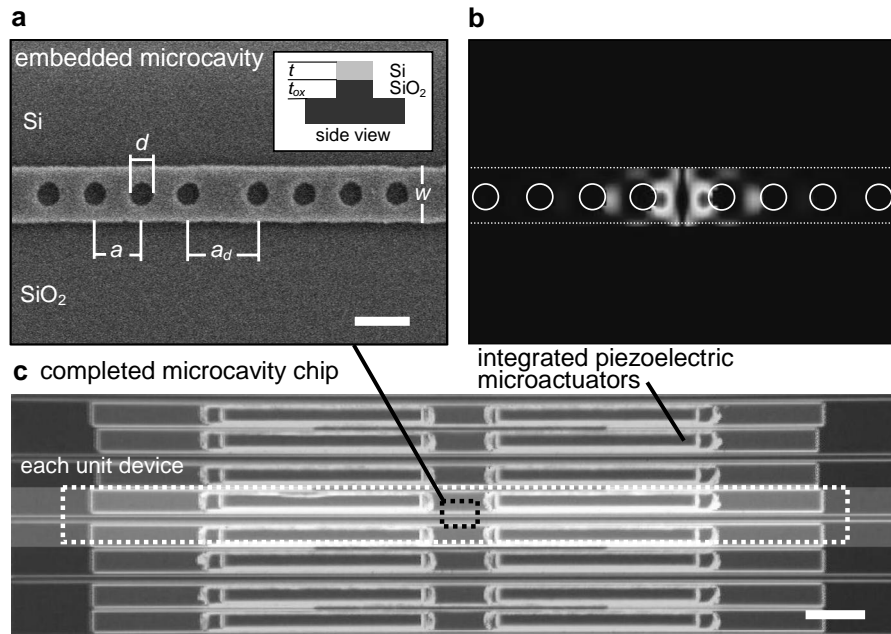


Fig. 2. Images of completed microcavity chip and numerical experiments on the field distribution. **a**, Scanning electron micrograph of the embedded microcavity patterned by X-ray lithography. Inset: side-view of Si waveguide on SiO₂ ridge. Scale bar: 500 nm. **b**, Electric energy distribution at middle 2D slice of microcavity, at resonance. **c**, Top view of completed strain-tunable microcavity with integrated piezoelectric microactuators. Scale bar: 100 μ m.

To study the effects of small strain (order 0.1% or less) on the microcavity, we employ first-order perturbation theory [7] to obtain a semi-analytical result for the strain-induced shift $\Delta\lambda$ in the resonant wavelength of the microcavity. First, the results of the 3D FDTD calculation are linearly interpolated to obtain the continuous fields on the dielectric interfaces. Next, a closed-form solution for the elliptical displacements of the dielectric interfaces is derived from classical mechanics [13]. The applied stresses are assumed to be free from discontinuities and the strain components are solved in polar coordinates with appropriate boundary conditions to obtain analytical expressions of the hole elliptical displacements. These displacements and the relevant fields are utilized to compute well-defined surface integrals of the unperturbed fields over the perturbed interface, as described by the perturbation theory. The results are repeated for various applied stress perturbations $\Delta\sigma$ to determine the corresponding resonance shifts $\Delta\lambda$. From a 3D FDTD computation, the shift in the transmission is presented in Figure 3b for an applied 0.2% strain. The unperturbed FDTD transmission of the microcavity is also shown for comparison. The transmission is normalized to the intensity at the band edges. The results predict a $\Delta\lambda$ of 8.4 nm (normalized for operation at 1.55 μm wavelengths) for an applied strain of 0.2%. While there are three components – hole ellipticity, defect length a_d and lattice constant a – in the strain perturbation, the major contribution is determined to be from changes in the defect length. A 2D computation gives a similar final result for $\Delta\lambda$, although the various contributions differ from the more accurate 3D computation. Other effects such as stress birefringence are found to be secondary, changing $\Delta\lambda$ by less than 1% fractional difference for applied strains on order 0.1%.

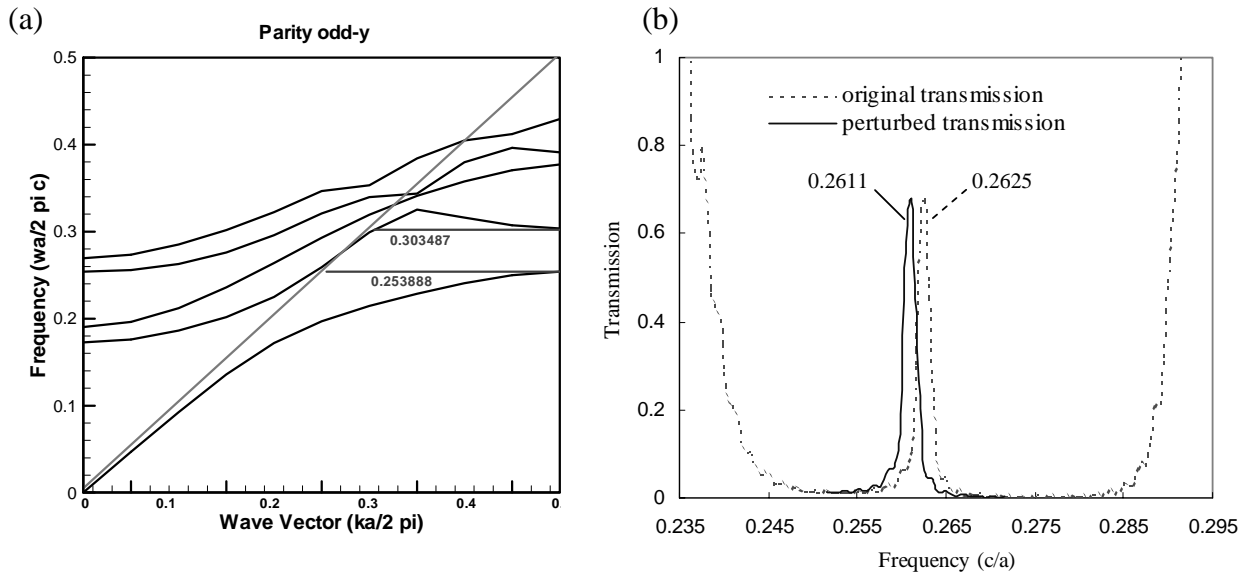


Fig. 3. (a) Band structure through 3D MPB computation [14]. (b) Computed transmission shift through first-order perturbation theory [7] and finite-difference time-domain in photonic band gap of the microcavity. The frequency is non-dimensionalized with lattice constant a and speed of light c .

3. DEVICE FABRICATION

The fabrication process has three major milestones: (1) aligned X-ray lithography along with waveguide processing for optical resonance detection with low transmission losses, (2) integrated thin-film lead zirconate titanate (PZT) processing with excellent quality piezoelectric properties, and (3) high yield membrane release with Si on top of membrane. PZT processing is designed before the X-ray lithography so that any yield issues with PZT processing will be shifted upstream and dealt with before X-ray waveguide processing and membrane release. This however requires etching of the PZT before annealing, as PZT cannot be annealed on top of a bare Si layer nor is there a reliable protective layer [15] which can be cleanly removed without attacking the 200 nm Si device layer. Membrane release possibilities include front-side XeF₂ etching or bulk KOH micro-machining from the backside. A combination of these two can be used to release a membrane with remaining Si for structural support against the oxide. Figure 4 summarizes the fabrication process.

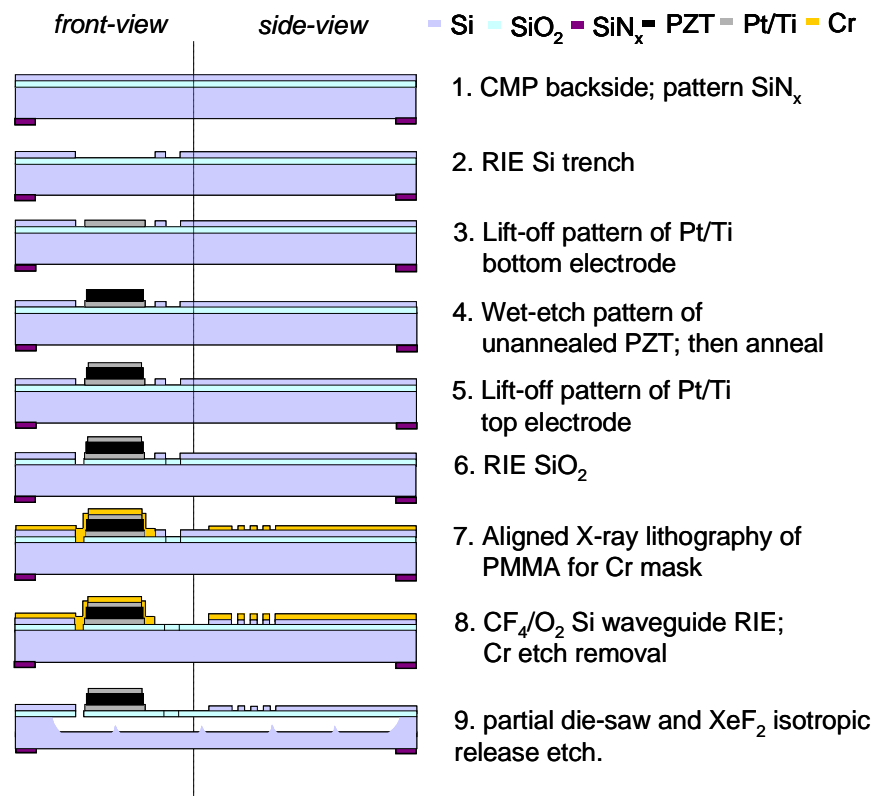


Fig. 4. Fabrication process flow schematic of strain-tunable photonic crystal waveguide.

The beginning substrate is a Silicon-On-Insulator Unibond wafer from SOITEC, chosen for low-loss transmission. The desired silicon device thickness is 184 nm, for resonance at 1.55 μm. Given the specialized wafers are single-side polished, we begin with a chemical mechanical processing step on the backside. PECVD silicon nitride is then deposited and patterned on the backside to permit the possibilities of using KOH bulk micromachining. The silicon device layer on the frontside is then etched to form the trenches for the thin-film PZT actuators. Subsequently, the bottom electrode is deposited with evaporation and lift-off processing. Thin-film PZT is then coated, dried and heated at 350 °C for pyrolysis, but left unannealed. Wet-etching is then employed to pattern the PZT before annealing at 650

°C. A Pt/Ti top electrode is then deposited with evaporation and lift-off processing. Oxide is reactive ion etched away at selective areas to permit a XeF₂ release later in the processing. X-ray nanolithography is then employed to pattern PMMA with 130 nm minimum features. Cr is evaporated and lift-off to form a hard mask for silicon etching to define the microcavity waveguide. After the silicon etching, the hard mask is removed with a Cr etchant. Resist is patterned above the waveguide to protect it during a later XeF₂ etch. The wafer is then partially die-sawed to allow eventual easy cleaving without breaking the membranes. A XeF₂ dry-etch is finally used to release the membrane, and the wafer cleaved to access the waveguide facets. Figure 2c shows the completed fabrication chip, with the PZT microactuators integrated with the microcavity.

4. EXPERIMENTAL RESULTS

A fiber lens assembly is used to couple two tunable laser diode sources into the prepared input and output waveguide facets, with wavelengths ranging from 1430 to 1610 nm. In addition, a stimulated emission broadband source is also used together with an optical spectrum analyzer to determine the optical spectrum. A piezoelectric-controlled stage with 10 nm resolution is used to direct the focused optical beam, with the appropriate polarization, into the sub-wavelength waveguide facets.

Waveguide losses are determined to be 5 – 7 dB/cm using a Fabry-Perot interference method [16], with 20 – 30 dB losses in the coupling between the fiber lens to the waveguide. The waveguide losses are primarily from the sidewall roughness, and the coupling losses are from mode size and shape mismatch, and impedance mismatch. The measured resonances are found between 1555 and 1570 nm for devices with different geometries, with quality factors Q ranging from 159 to 280. Figure 5 shows a specific resonance at 1555.2 nm, within the photonic band gap, and a measured Q of 159. The measurement

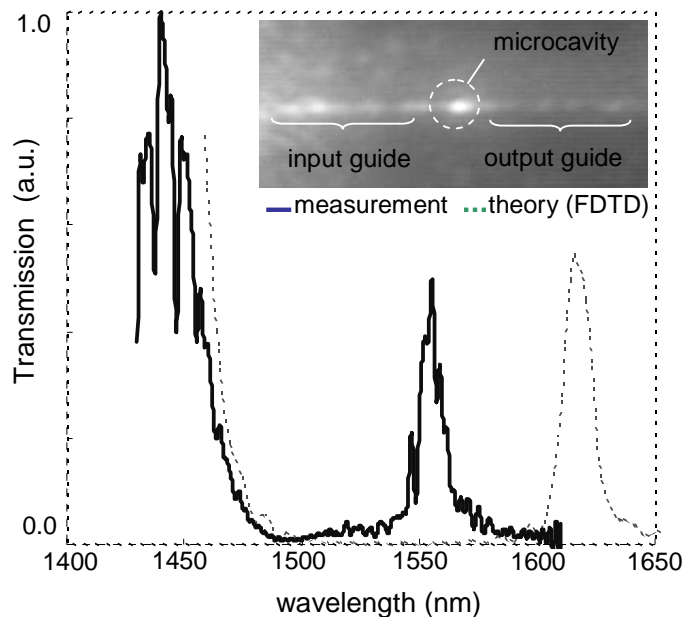


Fig. 5. Measured transmissions of the microcavity, depicting the band edge and resonance at 1555.2 nm with a Q of 159 ± 10 . The dotted lines depicted FDTD calculations, based on measured device dimensions. The superimposed shorter wavelength modulations on the transmission are from electron-beam stitching errors in the waveguide fabrication. Inset: imaged top view of microcavity with guidance in the waveguides.

compares well with our FDTD prediction, which shows a 3.8% fractional difference, within the numerical resolution of the FDTD and scanning electron microscope measurement resolution of the device dimensions.

When a DC bias is applied to the piezoelectric microactuators, the maximum $\Delta\lambda$ is determined to be +0.63 nm for 16 V (tensile stress) applied and -0.91 nm for 15 V (compressive stress) applied. Figure 6a shows the strain-tuned resonances for the various applied voltages. The fitted Lorentzians are generated through a trust-region nonlinear least squares (TRNLS) algorithm [17] with R^2 values of 0.94 ± 0.03 . For the particular dimensions of the microcavity, Q degrades by about 3% when the microcavity is under tension and improves when under compression. This is due to the dependence of Q on the field profile and position [18] in the band gap, both of which changes under the applied strain.

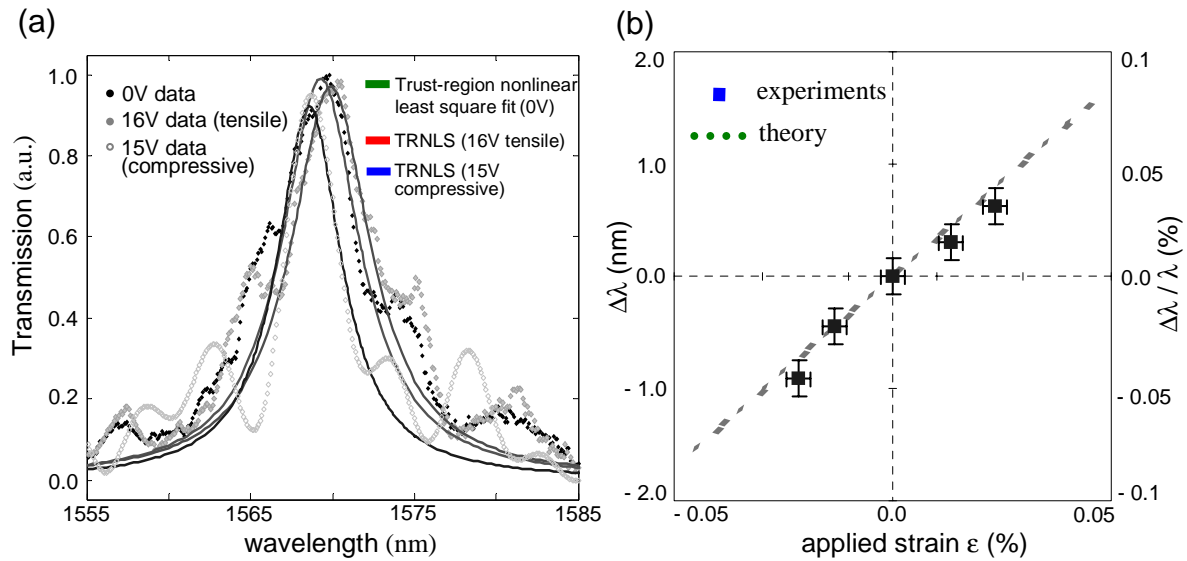


Fig. 6. Measurements and analysis of strain-tuned microcavity resonances. (a) Measured dynamic tuning of microcavity resonances under different DC-biased applied voltages, for tensile and compressive stresses to the microcavity. The shifts in resonance for each applied voltage are averaged over multiple measurements for each value of voltage. The variance in resonant wavelength, without any active tuning, is determined to be 0.02 nm from multiple measurements. (b) Comparison of strain-tuned experiments with first-order perturbation computations. The vertical error bars (± 0.17 nm) are from variations on the nonlinear least squares fitting algorithm; the horizontal error bars (2.7×10^{-3} %) are uncertainties in the Computer Microvision displacement measurements.

Figure 6b compares the measurements with the first-order perturbation predictions. The applied strain is estimated through Computer Microvision, an instrument that can measure displacement with nanometer precision [19]. The results are in excellent agreement: for an applied strain of 0.04%, first-order perturbation theory predicts a $\Delta\lambda$ of 1.55 nm while our experimental measurements show a $\Delta\lambda$ of 1.54 ± 0.17 nm. We expect, however, larger deviations for larger applied strains, since our predictions capture only the first-order perturbation [20].

5. CONCLUSIONS

We have designed, fabricated and characterized a tunable photonic band gap microcavity waveguide operating at 1.55 μm wavelengths to advance the concept of strain-tuning towards tunable photonic platforms. In this approach, we have employed thin-film piezoelectric microactuators. They permit: (1) sufficient force per voltage actuation to deform the periodic structures of interest, and (2) fine control of the tunability with sub-nanometer resolution. Moreover, compared to thermo-optics which commonly employed in tuning integrated optics devices, piezoelectric strain-tuning provides significantly low power consumption (on order of 30 nW at 10V) compared to thermal means, faster response times, and better localization for low cross-talk individual device tunability in high-density optical integrated circuits.

The strain-tuned photonic band gap microcavities demonstrate a resonant wavelength shift of 1.54 nm at telecommunication wavelengths of 1555 to 1570 nm. Operating at these wavelengths necessitates the use of more complex fabrication methods and tight device fabrication tolerances. X-ray lithography is used to define the microcavity resonator with a total device dimension on order of $3 \mu\text{m} \times 0.5 \mu\text{m}$. To predict the responses of a tunable microcavity, fully-vectorial electromagnetic computations are used together with first-order perturbation theory to understand the effects – the result is in good agreement with our experiments. Future developments include controlling the residual stress and thickness of the deformable membrane to permit larger strain at the optical elements of interests. Possible applications for the tunable photonic band gap microcavity include implementation of reconfigurable optical filters for network provisioning, and integration of the microcavity resonator towards tunable low-threshold lasers.

6. REFERENCES

1. S. Noda, M. Yokoyama, M. Imada, A. Chutinan and M. Mochizuki, *Science* **293**, 1123 – 1125 (2001).
2. H. Pier, E. Kapon and M. Moser, *Nature* **407**, 880 – 883 (2000).
3. J. Vuckovic, M. Loncar, H. Mabuchi and A. Scherer, *Phys. Rev. E* **65**, 016608 (2001).
4. S. W. Kim and V. Gopalan, *Appl. Phys. Lett.* **78**, 3015-3017, 2001.
5. C. W. Wong, P. T. Rakich, S. G. Johnson, M. Qi, Y. B. Jeon, E. P. Ippen, H. I. Smith, L. C. Kimerling, G. Barbastathis and S.-G. Kim, *Appl. Phys. Lett.* **84** (8), 1242 (2004).
6. J. S. Foresi, P. R. Villeneuve, J. Ferrera, E. R. Thoen, G. Steinmeyer, S. Fan, J. D. Joannopoulos, L. C. Kimerling, H. I. Smith and E. P. Ippen, *Nature* **390**, 143 – 145 (1997).
7. S. G. Johnson, M. Ibanescu, M. A. Skorobogatiy, O. Weisberg, J. D. Joannopoulos and Y. Fink, *Phys. Rev. E* **65**, 066611 (2002).
8. R. B. Apte, F. Sandejas, W. Banyai, and D. Bloom, Deformable Grating Light Valves for High-Resolution Displays, *Solid-State Sensor and Actuator Workshop*, Hilton Head, SC, 1-6 (1994).
9. G. B. Hocker, D. Younger, E. Deutsch, A. Volpicelli, S. D. Senturia, M. Butler, M. Sinclair, T. Plowman, and A. J. Ricco, The Polychromator: A Programmable MEMS Diffraction Grating for Synthetic Spectra, *Solid-State Sensor and Actuator Workshop*, Hilton Head, SC, 89-91 (2000).
10. X. M. Zhang and A. Q. Liu, A MEMS Pitch-tunable Grating Add/Drop Multiplexers, *Optical MEMS 2000 IEEE/LEOS International Conference*, Kauai, HI, 25-26 (2000).
11. D. E. Sene, J. W. Grantham, V. M. Bright and J. H. Comtois, Development and Characterization of Micro-Mechanical Gratings for Optical Modulation, *Proc. of 1996 IEEE Micro Electro Mechanical Systems Workshop*, San Diego, CA, 222-227 (1996).
12. C. W. Wong, Y. B. Jeon, G. Barbastathis and S.-G. Kim, Analog tunable gratings driven by thin-film piezoelectric microelectromechanical actuators, *Appl. Optics* **42**, 621-626 (2003).
13. Timoshenko, S. P. & Goodier, J. N. *Theory of Elasticity*, 2nd ed. (McGraw-Hill, New York, 1970).

14. Steven G. Johnson and J. D. Joannopoulos, Block-iterative frequency-domain methods for Maxwell's equations in a planewave basis, *Optics Express* **8**, no. 3, 173-190 (2001), <http://www.opticsexpress.org/abstract.cfm?URI=OPEX-8-3-173>.
15. The most possible candidate is silicon nitride to protect the Si when annealing PZT; however, dry or wet etches to remove the nitride will attack the 200 nm Si device layer, wherein the thickness is crucial to the guided mode wavelength.
16. R. Regener and W. Sohler, Loss in low-finesse Ti:LiNbO₃ optical wave resonators, *App. Phys. B* **36**, 143-147 (1985).
17. M. A. Branch, T. F. Coleman and Y. Li, A Subspace, Interior, and Conjugate Gradient Method for Large-Scale Bound-Constrained Minimization Problems, *SIAM J. on Scientific Computing* **21**, 1-23 (1999).
18. Johnson, S. G. & Joannopoulos, J. D. *Photonic Crystals: The Road from Theory to Practice* (Kluwer Academic Publishers, Norwell, 2002).
19. D. M. Freeman, A. J. Aranyosi, M. J. Gordon and S. S. Hong, Multidimensional Motion Analysis of MEMS using Computer Microvision, *Tech. Digest of Solid-State Sensors and Actuators Workshop*, Transducers Research Foundation (Cleveland Heights, Ohio), 150-155 (1998).
20. Higher-order perturbations suffer from the incomplete basis of our eigenproblem in terms of the electric field. However, we could cast the eigenproblem in terms of the magnetic field (such that $\nabla \cdot \mu \mathbf{H} = 0$ is satisfied) to compute higher-order corrections. Issues of fast-convergence, however, would need to be solved.